

PERFORMANCE OF A HIGHLY SENSITIVE, 19-ELEMENT, DUAL-POLARIZATION,
CRYOGENIC L-BAND PHASED ARRAY FEED ON THE
GREEN BANK TELESCOPE

D. ANISH ROSHI,¹ W. SHILLUE,¹ B. SIMON,² K. F. WARNICK,³ B. JEFFS,³ D. J. PISANO,^{4,5} R. PRESTAGE,² S. WHITE,²
J. R. FISHER,¹ M. MORGAN,¹ R. BLACK,³ M. BURNETT,³ J. DIAO,³ M. RUZINDANA,³ V. VAN TONDER,^{2,6} L. HAWKINS,²
P. MARGANIAN,² T. CHAMBERLIN,² J. RAY,² N. M. PINGEL,^{4,5} K. RAJWADE,^{4,5} D.R. LORIMER,^{4,5} A. RANE,^{4,5}
J. CASTRO,¹ W. GROVES,¹ L. JENSEN,² J. D. NELSON,² T. BOYD,¹ AND A.J. BEASLEY¹

¹*National Radio Astronomy Observatory (NRAO)^a,*

520 Edgemont Road, Charlottesville, VA 22903, USA

²*Green Bank Observatory (GBO)^b, 155 Observatory Rd,
Green Bank, WV 24944, USA*

³*Brigham Young University (BYU), Provo, UT 84602, USA*

⁴*West Virginia University (WVU), Dept. of Physics & Astronomy,*

P.O. Box 6315, Morgantown, WV 26506, USA.

⁵*Center for Gravitational Waves and Cosmology, WVU,*

Chestnut Ridge Research Building, Morgantown, WV 26505, USA.

⁶*Square Kilometre Array South Africa (SKA SA), Cape Town, South Africa.*

(Received; Revised; Accepted)

Submitted to ApJ

ABSTRACT

A new 1.4 GHz 19-element, dual-polarization, cryogenic phased array feed (PAF) radio astronomy receiver has been developed for the Robert C. Byrd Green Bank Telescope (GBT) as part of FLAG (Focal L-band Array for the GBT) project. Commissioning observations of calibrator radio sources show that this receiver has the lowest reported beamformed system temperature (T_{sys}) normalized by aperture efficiency (η) of any phased array receiver to date. The measured T_{sys}/η is 25.4 ± 2.5 K near 1350 MHz for the boresight beam, which is comparable to the performance of the current 1.4 GHz cryogenic single feed receiver on the GBT. The degradation in T_{sys}/η at $\sim 4'$ (required for Nyquist sampling) and $\sim 8'$ offsets from the boresight is, respectively, $\sim 1\%$ and $\sim 20\%$ of the boresight value. The survey speed of the PAF with seven formed beams is larger by a factor between 2.1 and 7 compared to a single beam system depending on the observing application. The measured performance, both in frequency and offset from boresight, qualitatively agree with predictions from a rigorous electromagnetic model of the PAF. The astronomical utility of the receiver is demonstrated by observations of the pulsar B0329+54 and an extended H II region, the Rosette Nebula. The enhanced survey speed with the new PAF receiver will enable the GBT to carry out exciting new science, such as more efficient observations of diffuse, extended neutral hydrogen emission from galactic in-flows and searches for Fast Radio Bursts.

Keywords: (cosmology:) large-scale structure of universe — (galaxies:) intergalactic medium — instrumentation: miscellaneous — ISM: individual (Rosette Nebula) — pulsars: individual (B0329+54) — techniques: imaging spectroscopy

Corresponding author: D. Anish Rosh, W. Shillue
aroshi@nrao.edu, bshillue@nrao.edu

^a The National Radio Astronomy Observatory is a facility of the National Science Foundation operated under a cooperative agreement by Associated Universities, Inc.

^b The Green Bank Observatory is a facility of the National Science Foundation operated under a cooperative agreement by Associated Universities, Inc.

1. INTRODUCTION

Radio Astronomy is primarily an observational science, in which high-sensitivity, large-scale surveys are an essential tool for new discoveries (Condon et al. 1998; Barnes et al. 2001; Manchester 2001; Bekhti et al. 2016; DeZotti et al. 2010). While large apertures enhance sensitivity they have a more limited field-of-view (FoV), when equipped with a single feed. The survey speed of a telescope is proportional to its FoV and the square of the signal-to-noise ratio required for the survey. In this paper, we describe a new 1.4 GHz (L-band) Phased Array Feed (PAF) system, built for the Robert C. Byrd Green Bank Telescope (GBT) as part of FLAG (Focal L-band Array for the GBT) project, which can enhance the FoV of the telescope by a factor of seven and has sensitivity comparable to the existing single feed 1.4 GHz receiver.

There are wide-ranging scientific interests to increase the FoV of the GBT near L-band. Here we focus on two scientific motivations. It is now known that galaxies must be accreting gas to sustain their star formation. With the current known gas content of galaxies, current star formation rates can be sustained only for a few billion years. However, there is evidence that the gas content of galaxies has remained roughly constant for the past 10 billion years, implying that galaxies must be accreting gas from the intergalactic medium (Prochaska, Herbert-Fort & Wolfe 2005). Current theories suggest that this accretion occurs in one of two modes: a hot mode where the gas is heated to 10^6 K, or a cold mode where gas remains below 10^5 K (Kereš et al. 2005, 2009; Sancisi et al. 2008). The cold mode, in particular, should be the dominant form of accretion for low mass galaxies in low density environments. Such accretion should be detectable via observations of neutral hydrogen at 21-cm (HI) at column densities of $N(\text{HI}) \lesssim 10^{18}$ cm² (Popping et al. 2009). To detect HI emission from the cold accretion flows from nearby galaxies, sensitive single-dish observations are essential (Chynoweth et al. 2008; Mihos et al. 2012; Wolfe et al. 2013; Pisano 2014; de Blok et al. 2014; Wolfe, Lockman & Pisano 2016). Since the expected line strengths are weak such surveys require enormous amounts of observing time. To reduce the observing time it is essential to increase the FoV of the telescope with high sensitivity multi-beam systems.

The discovery of Fast Radio Bursts (FRBs) has generated renewed interest in exploring the transient radio sky (Lorimer et al. 2007; Katz 2016). FRBs are bright, approximately millisecond duration individual pulses from compact sources exhibiting pulse dispersive delays over a wide bandwidth. The dispersive delays far exceed values expected from the interstellar medium of our Galaxy, indicating that they are extragalactic in origin. This has been confirmed by the localization and optical counterpart identification for FRB 121103, the only known repeating burst source (Chatterjee et al. 2017). So far about 24 FRBs have been detected (Petroff et al. 2016), with most of the detections made near 1.4 GHz. The physical nature and mechanism producing the burst are not known. Studies of such short duration radio transients are poised for a revolution with large FoV telescopes and flexible, high throughput backends (see, for example, Bannister et al. 2017).

The FoV of a radio telescope when equipped with a single feed is limited to the full width at half maximum (FWHM) of the primary beam, which is $\sim \lambda/D$, where λ is the observing wavelength and D is the aperture diameter of the reflector. The feeds are usually optimized to maximally receive radiation from the reflector while attenuate the ground spillover. The physical size of the feed is determined by this optimization process. Traditionally, the FoV of telescopes is increased by placing multiple such optimized feeds in the focal plane – referred to as a focal plane array (FPA). The physical separation between feeds in an FPA is determined by the size of the feeds. The large physical separation of the feeds results in non-overlapping beams on the sky. Further, the off-axis beams suffer efficiency degradation since the feed optimization is usually done for the central beam. Both of these effects result in a relatively poor mapping efficiency improvement.

In the last decade, the use of phased arrays employing a set of smaller focal plane radiating elements – referred to as phased-array feeds (PAFs) – has gained wide interest among the radio astronomy community (Fisher & Bradley 2000; Hay & Bird 2015; Warnick et al. 2016). In such PAF receivers, each element is electrically small, and thus does not optimally illuminate the reflector. However an optimal illumination with low spillover is obtained by the weighted sum of the amplified signal voltages from multiple elements. Multiple beams can be formed by adding signals with different sets of complex weights. The beams formed in this manner can be made to overlap, thus increasing the mapping efficiency. The design and optimization of PAFs are complicated by mutual coupling effects between elements (see, for example, Diao & Warnick 2017). The mutual coupling distorts the element beam pattern, and introduces channel-to-channel noise coupling between neighboring low-noise-amplifiers (LNAs) which follow these elements. Thus, accurate methods for electromagnetic modeling and beamforming are needed in order to achieve efficient performance.



Figure 1. (a) The 19 element dual-polarized dipole array. (b) The dipole and custom low-loss, low thermal conductivity transition to the low-noise amplifier.

Currently, PAFs are being developed for both single-dish radio telescopes and radio interferometers. Designing efficient PAFs require proper accounting of electromagnetic coupling and beamforming, which has led to new theories and techniques in PAF modeling (Woestenburg 2005; Warnick & Jensen 2007; Hay 2010). Further, several leading radio astronomy institutions have made significant progress on developing PAF receivers and systems. The Westerbork Synthesis Radio Telescope (WSRT) (Oosterloo, Verheijen & van Cappellen 2010) and the Australian Square Kilometer Array Prototype (ASKAP) (Hay & O’Sullivan 2008; Chippendale et al. 2015) have both built uncooled, broadband (> 800 MHz) PAFs near 1.4 GHz. The elements used by WSRT for their PAF, called the APERTure Tile In Focus (APERTIF), are Vivaldi antennas. The ASKAP Chequerboard PAF is made of a self-complementary connected element array (Hay & O’Sullivan 2008). A PHased Array feed Demonstrator (PHAD) has been developed by the Dominion Radio Astrophysical Observatory (DRAO) using Vivaldi elements (Veidt et al. 2011). Cryogenic PAF development is being pursued for the Arecibo telescope by the Cornell University (Cortes-Medellin et al. 2015) and for the Five hundred meter Aperture Spherical Telescope (FAST) (Wu et al. 2016); both have operating frequencies near 1.4 GHz. A higher frequency (70 – 95 GHz) PAF is also being developed by the University of Massachusetts (Erickson et al. 2015).

FLAG is a collaborative project between the National Radio Astronomy Observatory (NRAO), the Green Bank Observatory (GBO), Brigham Young University (BYU) and West Virginia University (WVU). During the first phase of the project, a prototype cryogenic ‘kite dipole array’ was built and tested successfully on the GBT (Roshi et al. 2015). In this paper, we present the construction of the next generation cryogenic PAF, and describe the measurement of its performance and comparison with a PAF model. The new PAF is optimized for the GBT optics to provide the required FoV, with a diameter of $\sim 20'$. Additionally, all of the instrumentation from the LNA to the backend was upgraded. A brief description of the new system is given in Section 2. For testing and commissioning of the system on the GBT, Nyquist-sampled voltage data were recorded in an instantaneous bandwidth of 300 kHz, and all signal processing was done off-line. The data processing method is described in Section 3. Before the system was installed on the GBT, the receiver temperature of the PAF was measured at the outdoor test facility at the GBO, as described in Section 4. The test observations made with the GBT are summarized in Section 5 and the results are given in Section 6. We have also observed a pulsar and an extended continuum source using the PAF system on the GBT. The results of these observations are presented in Section 7. The main results are summarized in Section 8. A GPU-based digital signal processing backend instrument has been realized for real-time calibration and beamforming by FLAG collaboration. This system will form the backend for the PAF for science observations with the GBT. The details of the real-time beamformer will be published elsewhere.

2. INSTRUMENTATION

The PAF consists of a hexagonal array of 19 dual-polarization dipole elements at ambient temperature connected to 19 pairs of cryogenic LNAs located in a vacuum dewar. Optimization of the design for maximum sensitivity over the antenna FoV of angular diameter $\sim 20'$, and across a bandwidth of 150 MHz, required adjusting the geometric

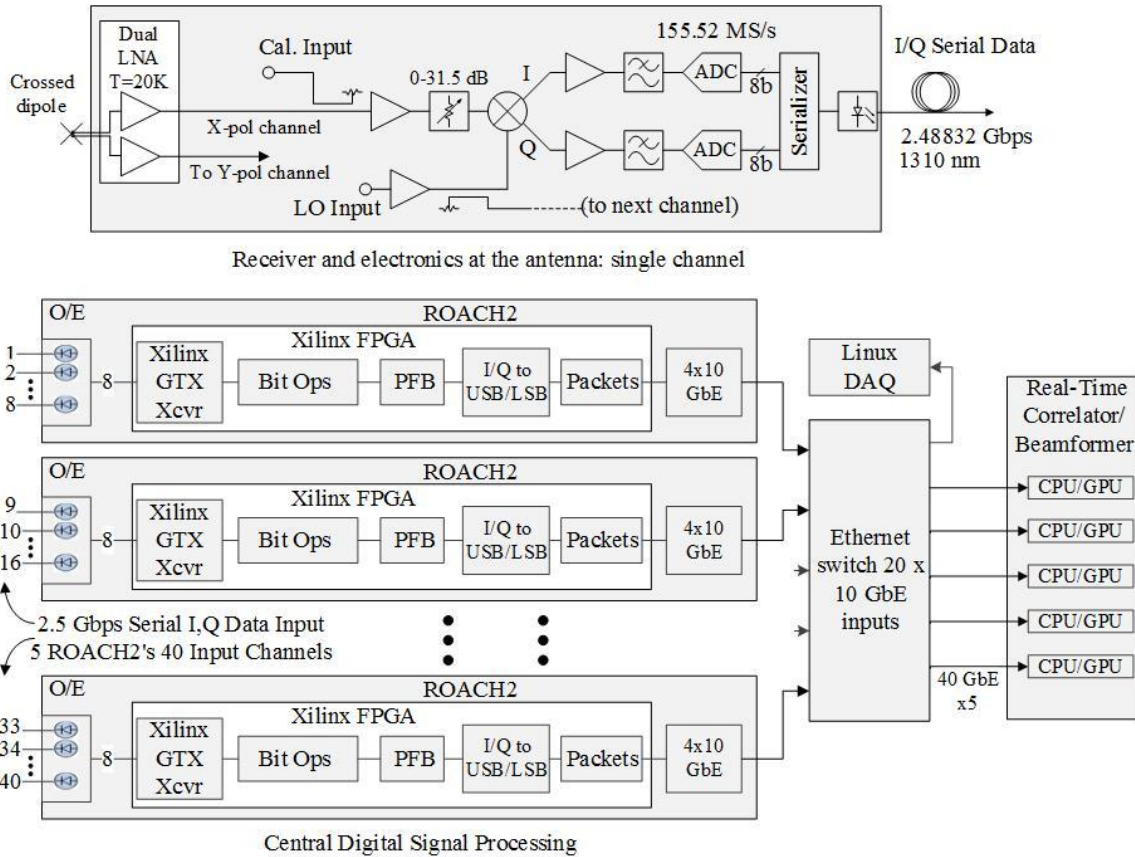


Figure 2. A block diagram showing the design of the phased array receiver system.

parameters of the dipoles which had been developed in prior work (Warnick et al. 2011). The optimal design is dependent upon the noise parameters of the LNA and uses maximum signal-to-noise ratio (S/N) beamforming as a parameter. The dipole array is shown in Fig. 1a. The dipoles were fabricated using brass and subsequently plated with copper (with thickness $\approx 6.35\mu\text{m}$) followed by $1\mu\text{m}$ of gold to reduce ohmic loss. An air-filled coaxial conductor transmission line was used to minimize dielectric loss. These vertical transmission lines function as a balun and a means of fixing the correct separation between the radiating elements and the ground plane. Two teflon beads located at either end of the transmission line center the inner conductor. Between the dipoles and the LNAs, which are located in the cryostat, there is a custom low-loss coaxial assembly that also serves as a thermal transition and a vacuum barrier, as shown in Fig. 1b. The LNAs use SiGe transistors selected for their low-noise performance at cryogenic temperatures (Weinreb et al. 2009). The measured average gain of the LNAs is 38 dB over their 1.2–1.7 GHz frequency range, and the median noise temperature is 4.85 K (the peak-to-peak variation in the measured values is 1.5 K), when operated at a physical temperature of 15 K (Groves III & Morgan 2017). A highly integrated, 40-channel electronics assembly encompasses all of the remaining functions of the receiver: calibration signal injection, warm post-amplification, power leveling, local oscillator distribution, down conversion, analog-to-digital conversion, and serial data transmission through optical fiber, as shown in Fig. 2. This post-amplification electronics assembly is the first deployment of a novel integrated unformatted digital link developed at NRAO (Morgan, Fisher & Castro 2013), which allowed the entire analog signal path and digitizers to be located directly behind the phased array. This reduced the power dissipation and minimized the physical footprint. We have confirmed many aspects of this new design including the methodology for recovering bit and word boundaries in the unformatted received data streams (Morgan & Fisher 2014). The digital link can be scaled in bit rate, bandwidth, and channel count for future PAF applications. The fiber optic link transports the samples over approximately 2 km to the Jansky Laboratory, to terminate in equipment racks containing

five ROACH2 FPGA boards¹, which perform bit and byte alignment, 512 channel polyphase filter bank, and sideband separation operations. The data from the spectral channels are re-quantized to eight bits, packetized and sent to an Ethernet switch through 10 GbE links. Only 500 spectral channels, selected by removing channels from the band edge, are sent to the switch. The data acquisition system developed for commissioning and testing consists of a Linux computer equipped with a high-speed disk, and connected to the switch through a 10 GbE link. The complex voltage samples from one of the spectral channels is recorded to the disk for offline processing.

The PAF and the associated receiver box are placed at the prime focus of the GBT. The GBT local oscillator (LO) system is used for the first down conversion. The digital down converters and the backend system are synchronized through a 10 MHz observatory-wide frequency reference, which is also used to lock the GBT LO system. The LO frequencies were set to 1550, 1450, 1350 or 1250 MHz for most observations since the sideband separation coefficients were previously calibrated for these LO values. For each LO setting, data were collected from a subset of 300 kHz PFB channels. The RF frequency corresponding to this subset of PFB channels was located within the 150 MHz bandwidth centered at the LO value.

For future science observations, a complete GPU-based digital signal processing back end instrument has been realized to process all 500 channels from the FPGA boards, covering 150 MHz bandwidth (see Fig. 2). It performs phased array calibration, beamforming, correlation, and pulsar and transient searches. It has several unique capabilities not found on other PAF-equipped telescopes. Array covariance matrices are saved continuously from the correlator as the primary data product. This enables post-correlation beamforming (Hay & Bird 2015) after the fact for spectral line or continuum observations, so that different beam forming weights can be applied to improve beam patterns, or to compute any desired number of overlapping beams on the sky (within the limits of the FoV accessible to the finite number of PAF elements). Also, we are in the process of developing software for two new operational modes: (a) a commensal mode, where a quick-dump real-time beamformed spectrometer runs concurrently with the correlator to permit opportunistic transient searches during observations of neutral hydrogen; (b) an RFI mitigation mode, where the correlator and real-time beamformer can be linked to form a tracking RFI nulling adaptive beamformer. This instrument was commissioned separately on the GBT in summer 2017, and the results will be presented elsewhere.

3. DATA PROCESSING AND PERFORMANCE METRIC

The offline processing of the recorded data proceeded with first taking a 64-point Fourier transform of the complex voltage time series, which provided a spectral resolution of $\sim 300/64 = 4.7$ kHz. The cross correlations between signals from all the 38 dipole outputs for each spectral channel were then computed and the correlation matrix \mathbf{R} was obtained as

$$\mathbf{R} = \frac{1}{N} \sum_{i=0}^{N-1} \mathbf{V}[i] \mathbf{V}[i]^H. \quad (1)$$

Here $\mathbf{V}[i]$ is the time series of complex voltage vector formed from the 38 dipole outputs from a spectral channel. The number of samples N used for the computation typically corresponds to an integration time of 5 s. The high spectral resolution is very useful to excise narrow band RFI. After RFI editing the cross correlations were averaged over 300 kHz bandwidth.

An offline post-correlation beamformer is implemented in a MATLAB² program (Jeffs et al. 2008; Hay & Bird 2015). For typical observations, the cross correlations on the source and at a nearby off-source position were measured. In this case,

$$S/N = \frac{\mathbf{w}^H \mathbf{R}_{\text{on}} \mathbf{w}}{\mathbf{w}^H \mathbf{R}_{\text{off}} \mathbf{w}} - 1, \quad (2)$$

where \mathbf{R}_{on} and \mathbf{R}_{off} represent the on-source and off-source correlation matrices respectively, and \mathbf{w} is the beamformer weight. The beamformer weights are obtained by maximizing the S/N, which will be the eigenvector corresponding to the maximum Rayleigh quotient. For forming beams at different positions in the FoV of the PAF system, the above procedure is repeated by moving the telescope and positioning the source appropriately.

We define the performance metric as the inverse of the maximum S/N when observing a compact astronomical source (Warnick & Jeffs 2008). As shown below, this inverse S/N can be expressed in terms of T_{sys}/η , if the flux density of the source is known, and it can be directly obtained from the observations of a compact source without making any

¹ https://casper.berkeley.edu/wiki/ROACH-2_Revision_2

² <https://www.mathworks.com/products/matlab.html>

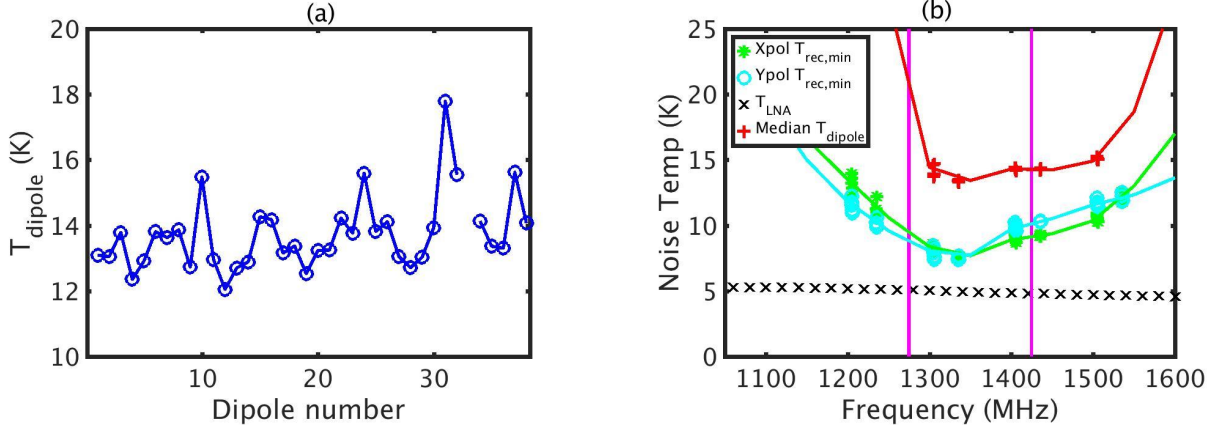


Figure 3. (a) Measured receiver temperature for the 37 dipoles near 1336 MHz. The dipoles numbered 1 to 19 correspond to X-polarization and 20 to 38 correspond to Y-polarization. The LNA connected to dipole 13 in Y-polarization was bad. (b) Median receiver temperature versus frequency with an interpolated curve are marked in red. The median value is obtained from the 37 dipole temperatures. The measured LNA noise temperature, T_{LNA} , is marked with a cross. The peak-to-peak spread in the measured LNA temperatures for the 37 amplifiers is about 1.5 K. The minimum receiver temperature $T_{rec,min}$ (see text) for the X and Y polarizations along with interpolated curves are shown in green and cyan. The minimum difference between $T_{rec,min}$ and LNA noise temperature is about 2.5 K, which we attribute to the losses ahead of the LNA. The vertical lines show the 150 MHz frequency range centered at 1350 MHz.

assumptions. This metric is useful to compare the performance of different PAFs. A nearby off-source position needs to be observed to derive T_{sys}/η and hence its value will depend on the diffuse foreground emission temperature at the off-source position. The measured value of $S/N = \frac{T_a}{T_{sys}}$, for the off-course system temperature T_{sys} and the excess antenna temperature

$$T_a = \frac{SA\eta}{2k}. \quad (3)$$

Here S is the flux density of the source, A is the physical area of the telescope aperture, k is Boltzmann's constant and η is the product of the aperture efficiency of the telescope and radiation efficiency of the PAF. Substituting in (3), we get:

$$\frac{T_{sys}}{\eta} = \frac{SA}{2k S/N_{max}}, \quad (4)$$

where S/N_{max} is the maximum S/N. We use the flux density of calibrator sources provided by Perley & Butler (2017). These flux densities are accurate to 3-5%.

4. RECEIVER TEMPERATURE

The receiver temperature of the PAF was measured at the outdoor test facility at the GBO. This facility is a small outdoor structure with a retractable roof facilitating hot and cold load measurements with the PAF receiver to obtain the receiver noise temperature by the Y-factor method (Warnick et al. 2010). The receiver is mounted with the dipoles facing up toward either an ambient temperature load (hot load) or the cold sky. A large aluminum cone, flaring upward from the edge of the dipole array, is attached to the receiver and functions to shield the dipoles from wide-angle ground radiation. To derive the Y factor, the array output voltage correlation \mathbf{R}_{hot} was measured with an absorber placed in front of the array, which forms an isotropic hot load at ambient temperature. A second correlation measurement \mathbf{R}_{cold} was made by pointing the array to a region of sky away from galactic plane, and this formed the cold load. In this case, the factor

$$Y = \frac{\mathbf{w}^H \mathbf{R}_{hot} \mathbf{w}}{\mathbf{w}^H \mathbf{R}_{cold} \mathbf{w}}, \quad (5)$$

and the receiver temperature

$$T_{rec} = \frac{T_{hot} - YT_{cold}}{Y - 1}, \quad (6)$$

where T_{hot} and T_{cold} are the temperatures of hot load and cold sky, respectively, and \mathbf{w} are the weights. The derived value of the receiver temperature depends on the weights, as seen from (5). The cold sky temperature is estimated

from the sky brightness temperature distribution and typically has a value of ~ 8 K (Delahaye, Gole & Waldteufel 2002). The hot load temperature is 296.5 K. Despite the use of the conical ground shield, the cold sky correlations were not devoid of contribution from ground scattered radiation. From single feed measurements using the outdoor test facility, it is estimated that a residual of ~ 4 K can be present in the receiver temperature values due to this scattered radiation.

Fig. 3a shows the measured receiver temperature T_{dipole} for each dipole. These temperatures are obtained using the Y-factor derived from the output power of each dipole in the array. Thus, for example, T_{dipole} for dipole 1 is equivalent to using $\mathbf{w}^T = [1, 0, 0, \dots, 0]$ (i.e. weight 1 for dipole one and 0 for all other dipoles) in (5) and then estimating the temperature using (6). This weighting scheme is applied for each dipole to get 38 T_{dipole} values (see Fig. 3a). The T_{dipole} values range between 12 K and 18 K near 1336 MHz. The missing value at dipole 13 in the Y-polarization is due to a bad LNA on that channel. The median value of T_{dipole} versus frequency is shown in Fig. 3b. The minimum T_{dipole} is about 13.3 K near 1336 MHz.

The measured T_{dipole} has contributions from ground scattering and mutual coupling between array elements. Since both of these contributions produce noise correlations at the output of the array, they can be canceled out to a large extent. This cancellation corresponds to the maximum Rayleigh quotient of Y, which will provide a minimum receiver temperature, $T_{\text{rec,min}}$. The weight vector that needs to be applied in (5) to get the maximum Y is the eigenvector corresponding to the maximum eigenvalue of the matrix $\mathbf{R}_{\text{cold}}^{-1}\mathbf{R}_{\text{hot}}$. Fig. 3b shows the $T_{\text{rec,min}}$ obtained from X- and Y-polarization data separately. The measured LNA noise temperature, T_{LNA} , versus frequency is also shown in Fig. 3b. The minimum difference between the measured LNA noise temperature and $T_{\text{rec,min}}$ is ~ 2.5 K near 1350 MHz. We attribute this excess noise temperature to any residual correlated noise and to losses ahead of the LNA, which include (a) loss in the dipoles and balun, (b) loss in the thermal transition and (c) connection losses. Thus the measured excess noise temperature provides an *upper limit* to the losses ahead of the LNA (i.e the loss in temperature should ≤ 2.5 K). In this paper, we assume that the losses ahead of the LNA are independent of the beamformer weights.

5. OBSERVATIONS

In March 2017, the phased array receiver was installed on the GBT. Extensive observations were made on a set of seven calibrator sources to measure the system performance. A list of observed calibrator sources, their J2000 coordinates, and flux density at 1350 MHz are given in Table 1. A log summarizing observations is given in Table 2. The observations can broadly be classified into two categories: (a) to measure the performance over the FoV; (b) to measure the boresight performance. The performance over the FoV was measured by observing on a grid of positions ('grid' observations) centered on the strong radio source Virgo A. The grid observation was made at 1336 MHz (bandwidth ~ 300 kHz). The grid positions were separated by $3'$ in both the elevation and cross-elevation directions. On-source and off-source measurements were made toward all calibrators in Table 1 to derive the boresight performance. The observed off-source positions have $+1^\circ$ offset in RA and 0° offset in DEC from the J2000 source positions. The

Table 1. Observed sources

Source	RA(2000) hh:mm:ss	DEC(2000) ° : ' : ''	$S_{1350\text{MHz}}$ Jy
3C123	04:37:04.4	+29 : 40 : 14	49.8
3C286	13:31:08.3	+30 : 30 : 33	15.4
3C147	05:42:36.1	+49 : 51 : 07	22.8
3C295	14:11:20.5	+52 : 12 : 10	23.2
3C48	01:37:41.3	+33 : 09 : 35	16.7
3C348	16:51:08.3	+04 : 59 : 26	49.5
Virgo A	12:30:49.6	+12 : 23 : 21	218.8

measurements were made over a set of frequencies ranging from 1200 MHz to 1500 MHz, each with a bandwidth of 300 kHz.

6. RESULTS

The grid observations are used to check the response of individual dipoles. Figs. 4 and 5 show the distribution of the S/N (as defined in (2)) but for a single dipole) obtained on Virgo A from each of the 19×2 dipoles (i.e. without forming beams). The peak S/N for the central dipole was about 2.6. As noted earlier, the dipole number 13 in Y-polarization was not functional. Dipole 14 in Y-polarization had a lower peak S/N compared to the central dipole by a factor of 2. This lower S/N is attributed to a faulty digital link. As discussed below, the two faulty dipoles have affected the results obtained from the Y-polarization data set.

6.1. T_{sys}/η over the FoV

A map of the T_{sys}/η is obtained from the grid observation data set by maximizing the S/N at each offset position. Figs. 6a and 6b show the distribution of T_{sys}/η as a function of elevation and cross-elevation offsets. The distribution is fairly symmetric about the center for the X polarization. The asymmetry seen in the Y polarization towards the south-west side is due to the faulty dipoles 13 and 14. The radial distributions (i.e. offset from the boresight) of the normalized T_{sys}/η for X and Y polarizations are shown in Figs. 7a and 7b. Only data points for elevation $\gtrsim -3'$ from those shown in Fig. 7b are used for making the radial distribution of Y polarization. The half power beam width at 1336 MHz is $\sim 10'$. The beam separation required for Nyquist sampling (i.e. $\lambda/(2D)$, where λ is the wavelength of observation and $D = 100$ m is the diameter of the GBT aperture plane; Padman (1995)) is $\sim 4'$. The degradation in T_{sys}/η at this offset is $\sim 1\%$.

The grid observations were used to examine the seven formed beam patterns. Fig. 8a shows the boresight maximum S/N beam measured using Virgo A and in Fig. 8b a beam with $5'$ offset from boresight is shown. The maximum S/N beams are smooth and approximately Gaussian for level between 0 and -10 dB. All of the seven formed beams show similar properties.

Table 2. Observation log

Date	Project	Description
dd-mm-yy	code	
08-03-17	TEST_08MAR2017	Measurement of receiver temperature LO ^a =1250,1350,1450,1550,1650,1750 MHz
11-03-17	TGBT17A_502.03	On-Off observations. Sources observed 3C123, 3C147, 3C48. LO=1350,1450 MHz
13-03-17	TGBT17A_502.05	On-Off observations. Sources observed Virgo A. LO=1350,1450 MHz
13-03-17	TGBT17A_502.06	Grid observations. Sources observed Virgo A. LO=1350 MHz
14-03-17	TGBT17A_502.07	On-Off observations. Sources observed 3C123, 3C147. LO=1250,1350,1450,1550 MHz
15-03-17	TGBT17A_502.08	On-Off observations. Sources observed 3C286, 3C295,3C348. LO=1250,1350,1450 MHz
16-03-17	TGBT17A_502.10	Sources observed 3C123, B0329+54, Rosette Nebula LO=1350 MHz

^aLocal Oscillator frequency

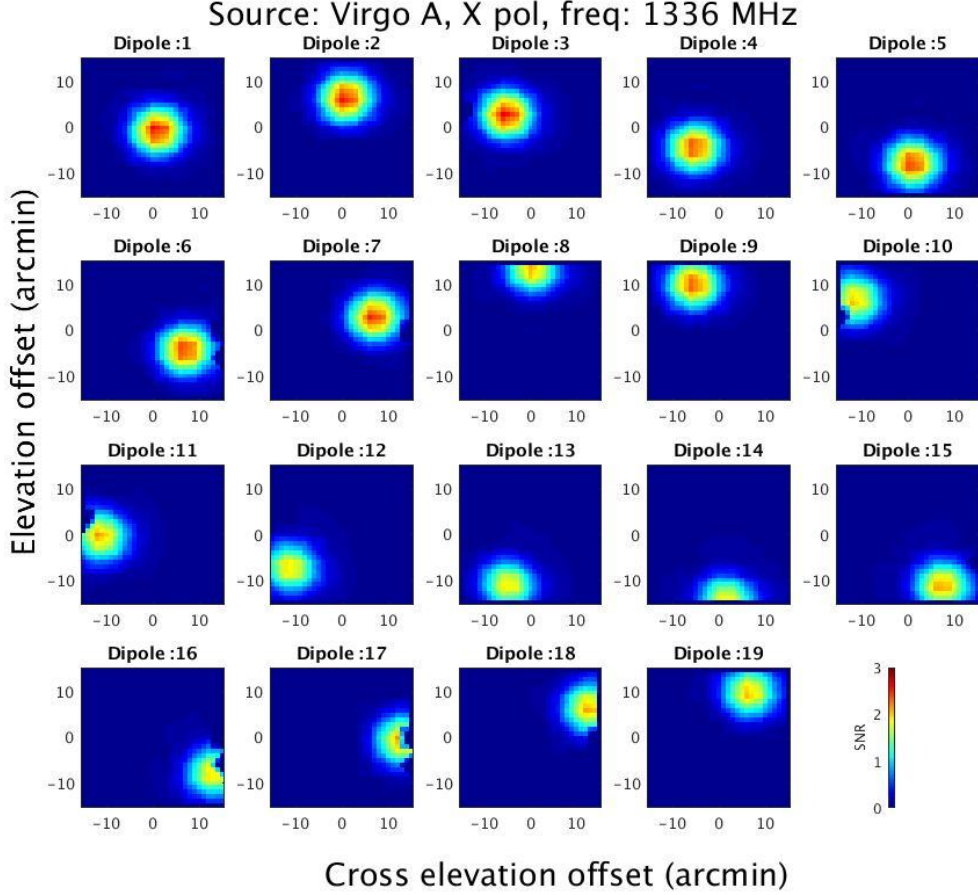


Figure 4. The S/N distributions at 1336 MHz in elevation and cross-elevation directions for each X polarization dipole obtained from grid observations.

6.2. Boresight T_{sys}/η

Plots of the measured boresight T_{sys}/η versus frequency for the two polarizations are shown in Figs. 9a and 9b. The data presented in these plots are from observations toward sources with flux density < 50 Jy. The weights for beamforming were derived by maximizing S/N on the observed source itself. The best median T_{sys}/η for X polarization is 25.4 K at 1336 MHz and the peak-to-peak spread in the values is ± 2.5 K. The scatter in X-polarization values are due to a combination of: (a) uncertainty in the flux densities of the sources; (b) variation in off-source sky contribution; (c) telescope pointing offset. The 3σ thermal noise uncertainty in all these measurements is ~ 0.3 K. The median T_{sys}/η increases by ~ 5 K near the edge of the 150 MHz bandwidth of interest, centered at 1350 MHz.

The median T_{sys}/η of Y polarization near 1336 MHz is 32.3 ± 5 K (peak-to-peak). To investigate the origin of the higher T_{sys}/η and the larger scatter of the Y-polarization measurement, we examine the observation toward 3C147 near 1336 MHz. The T_{sys}/η derived from this data set are 25 and 36 K for the X- and Y-polarizations, respectively. The normalized weight distributions obtained from this data set are shown in Fig. 10a and 10b. As seen in the figure, the weight distributions are centered near dipole 5, which is due to an uncorrected telescope pointing offset. Since dipole 13 and 14 in Y-polarization are faulty, the PAF is unable to form an optimum beam and hence the T_{sys}/η for the Y polarization is higher. We examined the data sets from all calibrators in the frequency range 1300 to 1400 MHz and found that a subset of the observations have telescope pointing offsets close to zero as inferred from the weight distribution (see Fig. 11a). The derived T_{sys}/η for this subset are similar for both polarizations and have values between 25 and 28 K. The weight distribution for the subset with $T_{\text{sys}}/\eta > 30$ K for Y-polarization is shown in Fig. 11b. As seen in the figure, the weight distribution is centered at dipole 5 for all the data in this subset. We conclude that the larger scatter and higher T_{sys}/η for Y-polarization compared to X-polarization is due to the telescope pointing offset

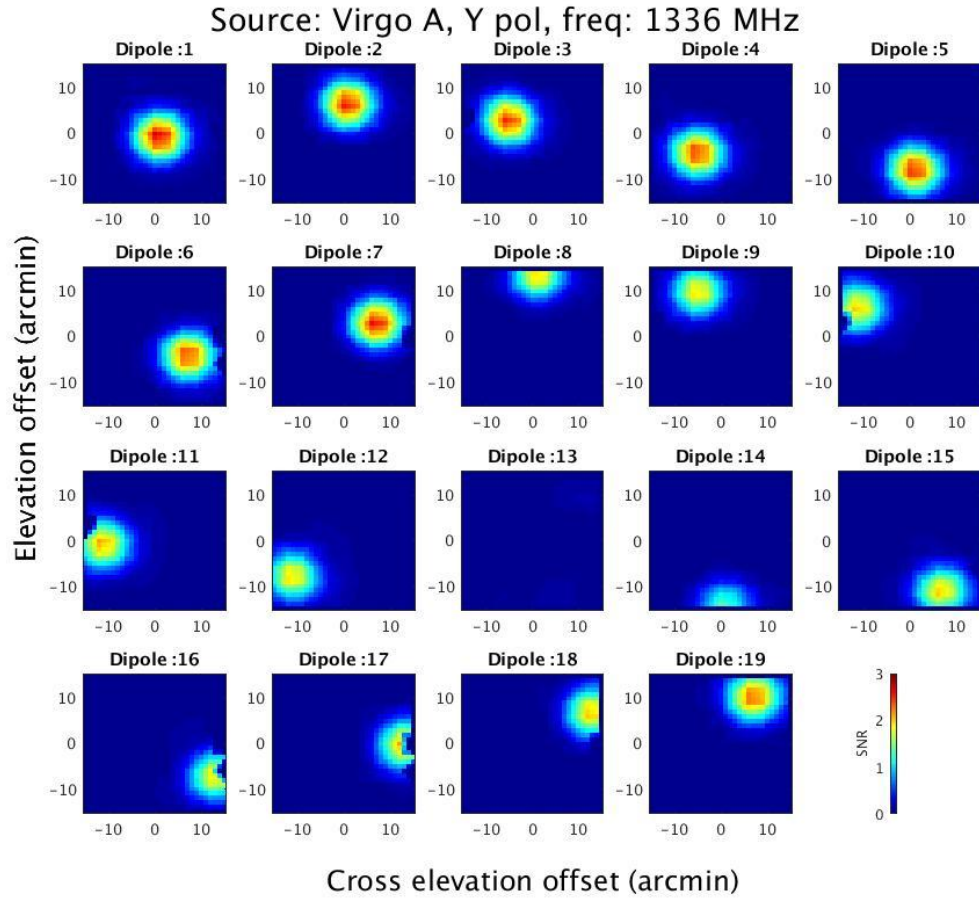


Figure 5. Same as Fig. 4 but for Y polarization. Dipole 13 has a faulty LNA and dipole 14 has peak S/N a factor of 2.0 lower than that of the central dipole due to a faulty digital link.

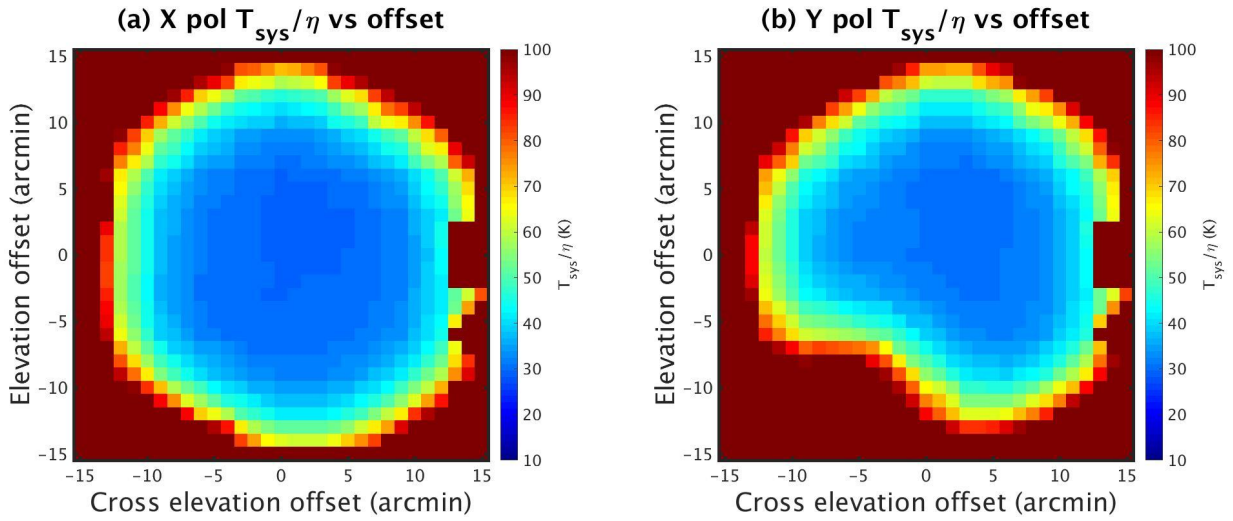


Figure 6. (a) Distribution of the T_{sys}/η in elevation and cross elevation directions for X-polarization obtained from Virgo A grid observations. (b) Same as (a) but for Y-polarization. The asymmetry seen in the south-west is due to faulty dipoles 13 and 14 (see text).

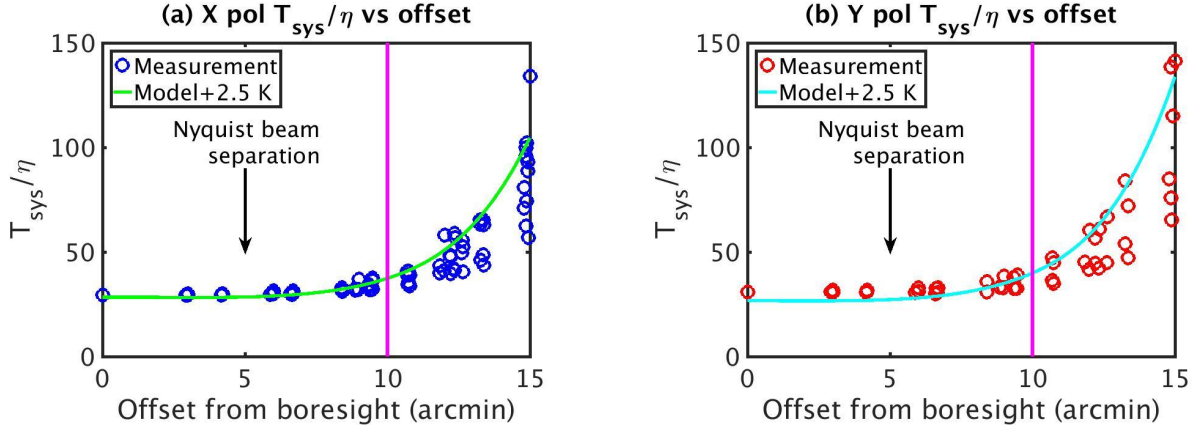


Figure 7. (a) The T_{sys}/η versus radial offset from the boresight for X-polarization are marked in circles. The half power beam width of $10'$ at 1336 MHz is marked by the vertical line. The PAF model prediction is shown by the solid line. The system temperature in the model is increased by 2.5 K to account for the loss ahead of the LNA (see Fig. 3b). (b) Same as (a) but for Y-polarization. Data points in Fig. 6b with elevation offset $> -3'$ are used for making the Y polarization plot.

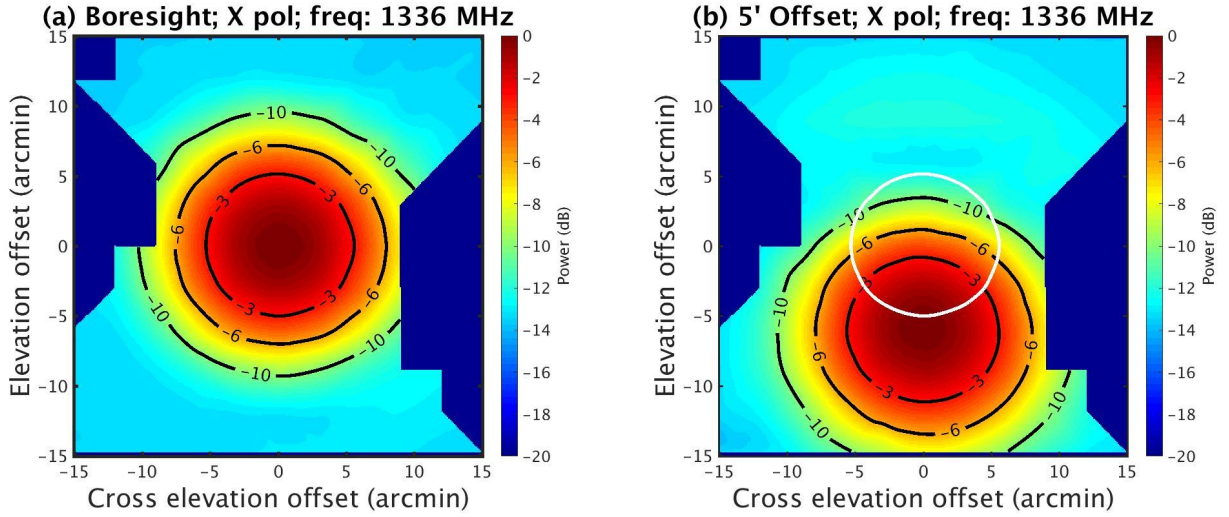


Figure 8. (a) Boresight beam formed using maximum S/N weights. The -3,-6 and -10 dB contours are marked. (b) An offset beam at about $5'$ south of the boresight direction. The -3,-6 and -10 dB contours are marked in black. The contour in white is same as the -3 dB contour of the boresight beam shown in (a). The dark blue regions on the left and right side of the plots are due to loss of data resulted from the applied cubic interpolation to make the figures.

and the presence of the two faulty dipoles. The large telescope pointing offset is because the GBT did not have an accurate pointing model for the PAF receiver system while we were doing the measurements.

The radio source Virgo A is the strongest calibrator source observed during the commissioning. The flux density of this source is 218.8 Jy at 1350 MHz. The best T_{sys}/η measured on this source are 28 and 30 K for the X and Y polarizations respectively. The 1σ noise is 0.3 K. These values are about 3 to 5 K higher than the median value obtained from sources with flux density < 50 Jy. A possible cause of this higher T_{sys}/η is the noise contribution due to the source itself (Anantharamaiah et al. 1991), which may be affecting the beamformer weight solutions.

We compare the performance of the PAF with the existing, cryogenic, optimized single feed 1.4 GHz receiver on the GBT, which has a $T_{\text{sys}}/\eta \sim 25.7 \text{ K}^3$. Our measurements show that the performance of the PAF system is comparable to this single feed receiver. Achieving comparable performance is a major milestone in the development of the PAF. Table 4 lists the T_{sys}/η of multi-beam receivers in other telescopes for comparison.

³ <https://science.nrao.edu/facilities/gbt/proposing/GBTpg.pdf>

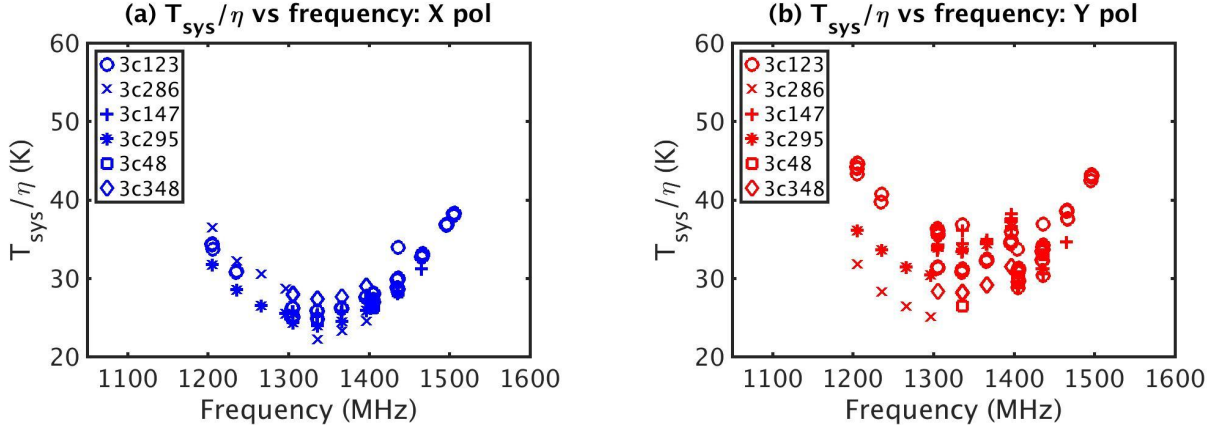


Figure 9. The T_{sys}/η for boresight beam obtained from observations with the PAF on the GBT for X-polarization (a) and Y-polarization (b). The sources observed are indicated in the legend.

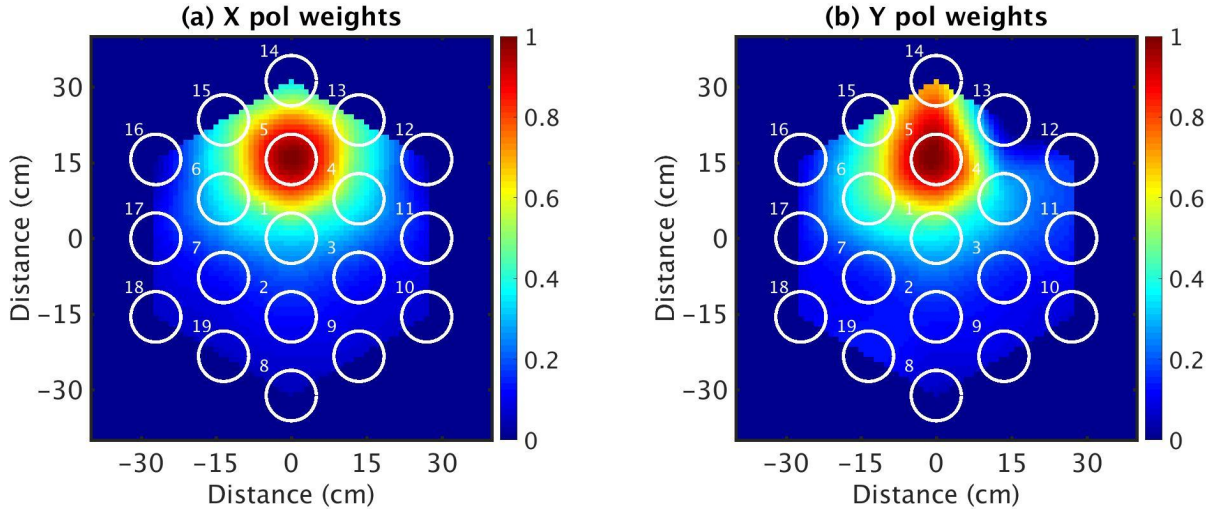


Figure 10. The normalized weight distributions obtained from 3C147 observations near 1336 MHz for X and Y polarizations are shown in (a) and (b). The distributions are superposed on the dipole array geometry; the white circles show the location of the dipoles. These plots illustrate the reason for higher T_{sys}/η and larger spread in the measured values for Y polarization. The T_{sys}/η for the Y-polarization obtained from the 3C147 data set is 36 K and that for X-polarization is 25 K (see Fig. 9). The distribution of weights is centered on dipole 5 due to the telescope pointing offset. Dipoles 13 and 14 (both are faulty dipoles) in Y-polarization are needed to get the optimum T_{sys}/η . Thus the higher T_{sys}/η for the Y polarization compared to the X-polarization in this measurement is due to the faulty dipoles.

6.3. Survey speed

The intrinsic survey capability per unit bandwidth of an astronomical receiver is found by evaluating the squared sensitivity integral given in (Hay & Bird 2015, Eq. 83),

$$\text{SSFoM} = \int \mathcal{S}^2(\Omega) d\Omega \quad (7)$$

where the sensitivity map $\mathcal{S}(\Omega)$ is the receiver sensitivity as a function of sky angle Ω . By dividing the survey speed figure of merit, SSFoM, by the peak sensitivity, the survey speed weighted field of view, SSFoV, of the instrument can be found as

$$\text{SSFoV} = \frac{1}{\mathcal{S}_{\text{max}}^2} \int \mathcal{S}^2(\Omega) d\Omega \quad (8)$$

The PAF sensitivity map is measured by steering the telescope to place a bright calibrator source at each of a grid of closely spaced points in the sky, measuring the realized sensitivity of the receiver with the source at that location, and

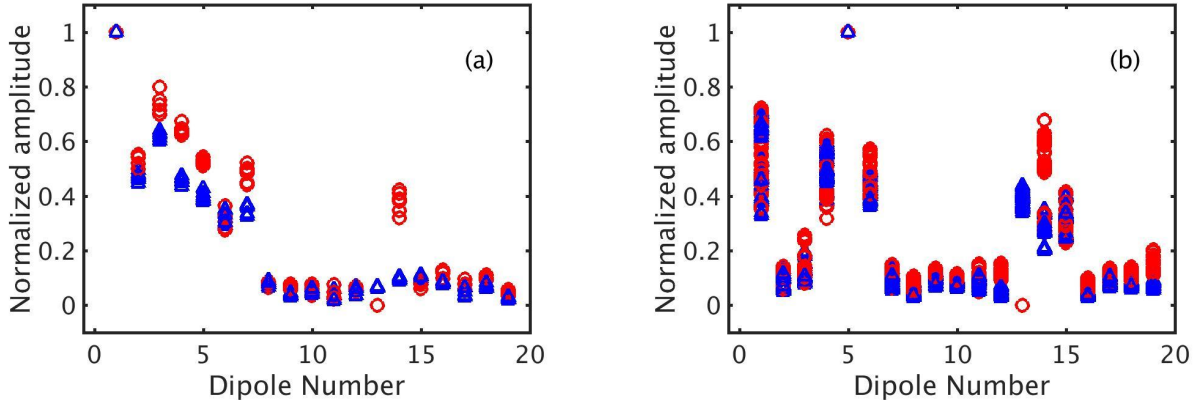


Figure 11. (a) Normalized weights (blue - X polarization; red - Y polarization) obtained from a subset of measurements shown in Fig. 9 where the weight distribution is centered at dipole 1. For this subset of measurements the T_{sys}/η for both X and Y polarizations are comparable. (b) Normalized weights for the subset of data with $T_{\text{sys}}/\eta > 30$ K for Y-polarization in the frequency interval 1300 to 1400 MHz (see Fig. 9b). The weight distribution for all these measurements are centered near dipole 5.

thereby sampling the sensitivity map at many discrete points. The integrals in SSFoM and SSFoV are approximated as sums over the sample points. These figures of merit are quite general, and can be used to compare single-pixel receivers, cluster feeds, phased array feeds, and aperture arrays on an equal footing.

To remove the dependence of the field of view on dish size, and obtain a dimensionless number that allows instruments with different aperture sizes to be compared more easily, the survey speed weighted field of view is commonly expressed as a number of beams. The angular field of view is divided by the area of the sky per beam when fully sampled by independent, formed beams to obtain

$$N_b = \frac{\text{SSFoV}}{\Omega_b} = \frac{\text{SSFoM}}{\Omega_b \mathcal{S}_{\text{max}}^2} \quad (9)$$

The amount of beam overlap required for full sampling, which determines the value of the area Ω_b per fully sampled beam, is treated in Hay & Bird (2015). While (7) is the primary definition of SSFoM, the number of beams in (9) is quite convenient and widely used in comparing various types of instruments.

6.3.1. Practical survey speed with real time beamforming

The field of view expressed as a number of independent beams N_b as in (9) is generally not equal to the number of beams that are formed in signal processing. The above considerations apply to the intrinsic survey speed of the analog receiver front end. When the digital back end is included in the analysis, the survey speed of an instrument may be limited further in the signal processing when the receiver back end operates in real time beamforming mode. To reduce hardware costs, fewer beams than are required to fully sample the field of view may be formed. In this case, the practical survey speed of the instrument is lower than the intrinsic SSFoM in (7).

In other cases, such as array receivers with signal processing back ends that allow post-correlation beamforming, in certain observing modes more beams may be formed than are required to fully sample the field of view. In this case, the number of formed beams is greater than N_b in (9). If the formed beams overlap, there is correlation between the signal and noise from beam to beam and the information provided by the beams may not be independent.

In view of the complex relationship between the field of view expressed as a number of beams and the number of beams that are formed in digital signal processing, there are differences in the assumptions made in the reported number of beams from one instrument to another. Despite the ambiguity, field of view as number of beams is so convenient a metric, and so generally used in the community, that we accept the disadvantages of this way of parametrizing field of view and provide comparison values, while stating as carefully as possible the assumptions made in the calculation.

To analyze the practical survey speed with a given number of formed beams, we consider three observing cases, which are typical applications of a PAF system on a telescope.

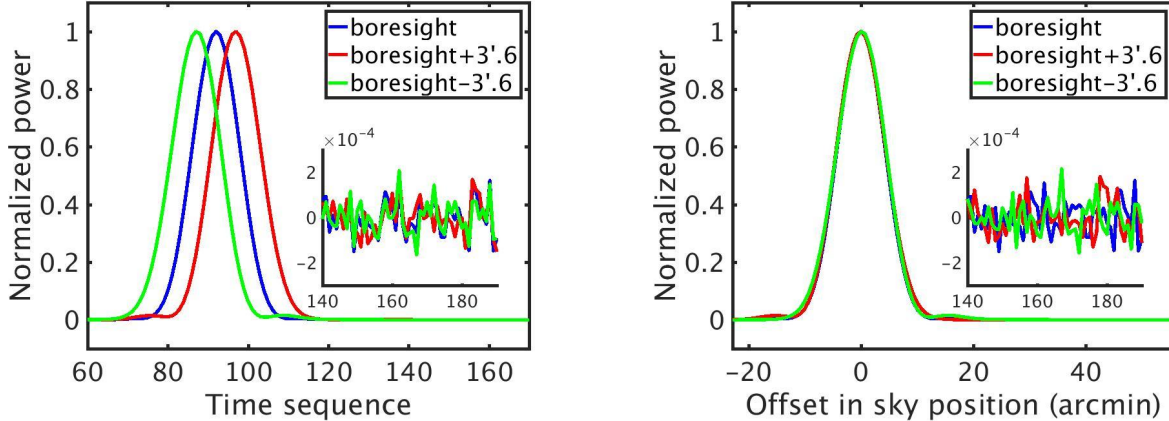


Figure 12. (a) Normalized power vs time from the three beams of the PAF in an observing scan made towards Virgo A. The two off-boresight beams are separated by about $3'.6$ (approximately Nyquist spacing) on either side of the boresight beam. The inset shows the data from the three beams in the off-source region. The correlation of the noise fluctuations from the three beams are evident. The axes of the inset have the same units as the main figure axes. (b) Normalized power vs sky position from the three beams of the PAF after aligning the data in sky coordinates. The inset shows the data from the three beams in the same off-source region as in Fig. 12a. As can be seen, the noise is no longer correlated (i.e. $\rho_{m,n} = 0$ for $m \neq n$) and the RMS in the averaged data from the three beams reduces by $1/\sqrt{3}$ as expected for an uncorrelated noise.

1. Survey observations that do not require averaging of data simultaneously obtained from the different beams. Examples for this observing case are searching for pulsars and HI observations of objects with angular size smaller than the FWHM beam size.
2. Imaging a region of the sky with the PAF system. HI and continuum imaging of extended sources are examples for the second case. Performing such observations with the PAF in the On-The-Fly (OTF) mode has some advantages, for example, to reduce the telescope pointing overhead. Averaging data obtained from different beams in an OTF observation can optimize the survey speed. However, the sky position needs to be aligned before averaging the images from the different beams, which makes the noise in each pixel of the images uncorrelated. This is demonstrated in Fig. 12 using a 1D scan toward Virgo A obtained with FLAG.
3. Some observations require averaging of data simultaneously obtained from the different beams. An example for such case is imaging of HI emission from an extended source and then smoothing the image to obtain a low angular resolution ($>$ FWHM beam width) spectrum. The noise correlation between beams will result in a spatial correlation of noise in the image and hence the S/N will not improve by the square root of the number of pixels averaged. As discussed below, this class of observations will benefit by keeping the PAF beams at twice the Nyquist separation or more.

Survey speed metrics for each of these observation cases will be given in the next section.

6.3.2. Effective number of beams

In a PAF system, if a large number of highly overlapping beams were formed in signal processing, the beams would be highly correlated, and little new information could be gleaned from adjacent beams. This manifests as strong signal and noise correlation between beams. Further, the sensitivity of each formed beam will differ because of the correlation of receiver noise between elements in the PAF. Following closely the intrinsic number of beams defined by (9), we develop in this section a figure of merit, in a practical sense, that measures the field of view of the PAF with a given number of formed beams, the *effective number of beams*.

Survey speed is determined by the time required to integrate an image such that the sensitivity in each pixel is higher than some desired sensitivity. We consider surveying a region of the sky of angular size Ω_s sampled at Ω_b , the independently sampled beam area in (9). The number of pointings that need to be made for such an observation is Ω_s/Ω_b . Imaging speed can be improved with a multi-beam system by moving the telescope so that the region of interest is observed in each beam and then averaging the images obtained from different beams. As discussed above,

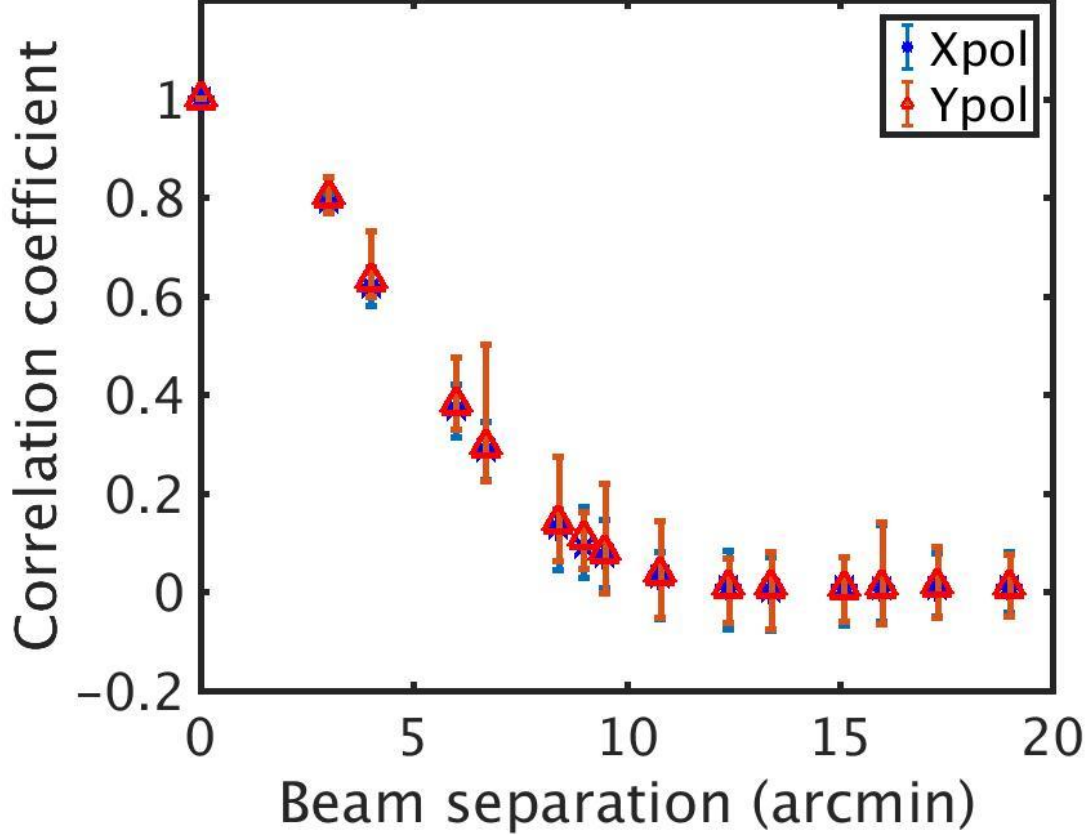


Figure 13. Calculated noise correlation between beams of FLAG as a function of beam separation. The ‘error bar’ represents the peak-to-peak range in the calculated values.

for observing cases 1 and 2, the noise correlation between the beams does not affect the net sensitivity of the averaged image. However, the sensitivity of the beams are different, which need to be taken into account in the survey speed calculation. The effective number of beams for such applications is defined as

$$N_{\text{effb}} = \frac{1}{\left(\frac{A \eta}{T_{\text{sys}}}\right)_{\text{max}}^2} \sum_{n=1}^{N_{\text{beam}}} \left(\frac{A \eta_n}{T_{\text{sys},n}}\right)^2 \quad (10)$$

where A is the physical area of the telescope, $\frac{A \eta_n}{T_{\text{sys},n}}$ is the ratio of the effective area of the telescope to the system temperature for beam n and $\left(\frac{A \eta}{T_{\text{sys}}}\right)_{\text{max}}$ is the maximum value of $\frac{A \eta_n}{T_{\text{sys},n}}$. The survey speed figure of merit is

$$\text{SSFoM} \approx N_{\text{effb}} \left(\frac{A \eta}{T_{\text{sys}}}\right)_{\text{max}}^2 (\theta_b)^2 \quad (11)$$

where θ_b is the square root of the independent beam area, which from the treatment of Hay & Bird (2015) is $\lambda/(2D)$.

For observing case 3, we must first determine the beam to beam noise correlation, as represented in the fluctuations in the estimated power at the output of a formed PAF beams. We estimate the correlation coefficient as

$$\rho_{n,m} = \frac{\langle (P_{B_n} - \bar{P}_{B_n})(P_{B_m} - \bar{P}_{B_m}) \rangle}{\sqrt{\langle (P_{B_n} - \bar{P}_{B_n})^2 \rangle \langle (P_{B_m} - \bar{P}_{B_m})^2 \rangle}} \quad (12)$$

Here

$$P_{B_n} = P_{B_n}[j] = \mathbf{w}_n^H \mathbf{R}[j] \mathbf{w}_n, \quad (13)$$

$$P_{B_m} = P_{B_m}[j] = \mathbf{w}_m^H \mathbf{R}[j] \mathbf{w}_m \quad (14)$$

are the time series of the power from beam n and m , respectively, estimated from the time series of the correlation matrices $\mathbf{R}[j]$ after multiplying it with the beamformer weights \mathbf{w}_n and \mathbf{w}_m for the two beams. The expectations of P_{B_n} and P_{B_m} are obtained as

$$\bar{P}_{B_n} = \frac{1}{M} \sum_{j=0}^{M-1} P_{B_n}[j], \quad (15)$$

$$\bar{P}_{B_m} = \frac{1}{M} \sum_{j=0}^{M-1} P_{B_m}[j]. \quad (16)$$

The angle brackets in (12) indicate time average over M samples. A plot of the calculated noise correlation between the boresight beam and the off-boresight beams of FLAG as a function of beam separation is shown in Fig. 13. The noise correlation is obtained from the off-source data. The correlation drops by about 60% at the Nyquist beam separation ($\sim 4'$) and it drops to $\sim 15\%$ at twice the Nyquist beam separation.

The beam to beam noise correlation will result in a spatial correlation of noise in the image made with a PAF. For a given beam spacing, the spatial correlation coefficient of the noise in the image will be same as that given by (12) even though the correlation coefficient is obtained by time average (the underlying stochastic process is ergodic in nature). A lower angular resolution image needs to be made for the third class of applications, but the S/N of the image will not improve by the square root of the number of pixels averaged during smoothing. The improvement in S/N depends on the angular resolution to which the image is smoothed. For the specific case when the image is smoothed to an angular resolution approximately equal to SSFoV (see (8)), the final noise variance is

$$\sigma^2 = \frac{1}{N_{\text{beam}}^2} \sum_{m,n}^{N_{\text{beam}}} \sigma_m \sigma_n \rho_{n,m} \quad (17)$$

where σ_m, σ_n are the RMS noise fluctuations in beams m and n , respectively, $\rho_{n,m}$ is the correlation coefficient of the noise in beams m and n (see (12)) for the beam spacing used for the survey. The survey speed is inversely proportional to this noise variance. Approximating the sensitivity of the beams as equal and factoring the resulting survey speed as in (9) leads to the effective number of beams

$$N_{\text{effb}} = N_{\text{beam}} \left(\frac{1}{N_{\text{beam}}} \sum_{m,n}^{N_{\text{beam}}} \rho_{n,m} \right)^{-1} \quad (18)$$

If the correlation $\rho_{n,m}$ vanishes for $n \neq m$ (i.e., the noise is uncorrelated between beams), the number of effective beams is equal to the number of formed beams, as expected. Thus, the third class of observing application will benefit by keeping the beams at twice the Nyquist separation or more since $\rho_{n,m}$ is smaller for larger beam spacing (see Fig. 13).

6.3.3. Survey speed comparisons

The SSFoMs of FLAG, obtained using (11), with 7 beams spaced at Nyquist separation ($\sim 4'$) and twice Nyquist separation ($\sim 8'$) are listed in Table 3. A major use of the new PAF system on the GBT will be to observe extended H I emission from nearby galaxies. These observations will be typically done in the OTF mode and fall into the first and second category of observations mentioned above. The T_{sys}/η of FLAG is optimum near 1350 MHz and it degrades by a factor of ~ 1.1 near 1.42 GHz. Thus the SSFoMs for H I observations are 2184 and 1640 $\text{deg}^2 \text{ m}^4 \text{ K}^{-2}$ for the two beam separations (see Table 3), which are a factor of 5.3 and 4 higher than the GBT single-feed receiver. A comparison of the SSFoM of FLAG, the existing GBT single-feed receiver, and our estimated values for multi-beam receivers at other telescopes, is given in Table 4. We computed the intrinsic SSFoM (see (7)) of FLAG using the data shown in Fig. 6a, which is about 10690 $\text{deg}^2 \text{ m}^4 \text{ K}^{-2}$. The derived SSFoV using (8) shows that about 25 beams need to be formed in the signal processing backend to obtain the full survey capability of FLAG (see Table 4).

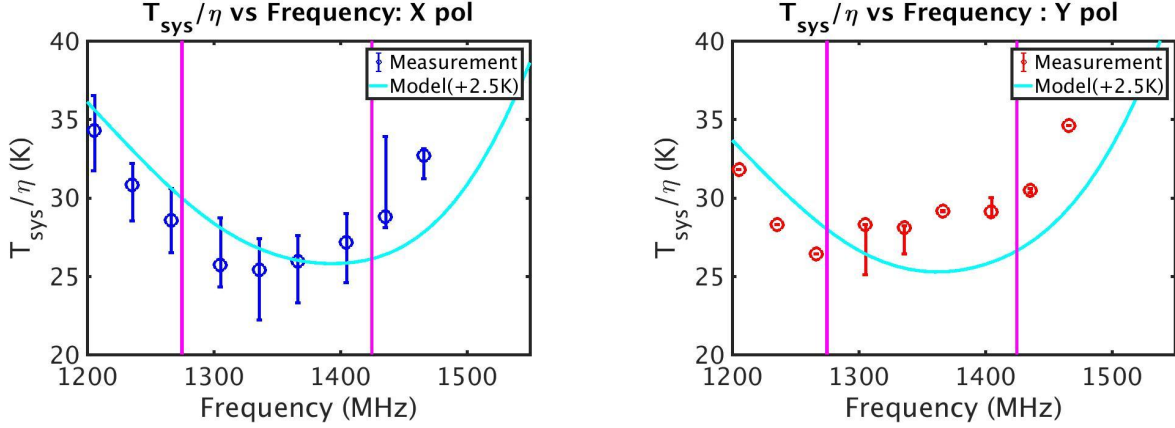


Figure 14. The PAF model prediction (solid line) along with the median measured T_{sys}/η with their peak-to-peak variation for X (left) and Y (right) polarizations. The data points shown in Fig. 9 are used to compute the median T_{sys}/η . The median is computed from the set of measurements in a frequency interval of ~ 1.5 MHz. The model assumes loss-less PAF and hence the system temperature in the model is increased by 2.5 K to take into account of the losses ahead of the LNA (see Fig. 3b).

For broadband observations (for example, pulsar observations), the survey capability of an instrument scales with the signal processing bandwidth. The real-time beamformer backend for FLAG will have a bandwidth of about 150 MHz. The mean value of T_{sys}/η for the 7 beams over this bandwidth is about 28 K for Nyquist beam separation. The SSFoM scaled by bandwidth is $3.6 \times 10^5 \text{ deg}^2 \text{ m}^4 \text{ K}^{-2} \text{ MHz}$. For the GBT single feed L-band system the usable bandwidth is about 400 MHz (after removing the RFI effected bands). Assuming a constant T_{sys}/η over the 400 MHz bandwidth of the GBT, the survey speed of the single feed system is $1.7 \times 10^5 \text{ deg}^2 \text{ m}^4 \text{ K}^{-2} \text{ MHz}$. The SSFoM bandwidth product of FLAG is about 2.1 times larger than the GBT single feed system for pulsar or other broadband applications.

6.4. Comparison with the PAF model, system parameters and FoV

For high-sensitivity receivers, further reductions in system noise become increasingly challenging as the system performance improves. This is especially true for phased array receivers, for which mutual coupling effects require a

Table 3. Survey speed of FLAG^a

Receiver System	θ_b^b (')	T_{sys}/η^c (K)	N_{effb}^d	SSFoM (deg ² m ⁴ K ⁻²)	Notes/Ref
FLAG (Nyquist)	4	25.4, 25.7	6.9	2924	1,2
FLAG (2 x Nyquist)	4	25.4, 30.5	5.2	2195	1,3
FLAG (HI, Nyquist)	3.8	28.0, 28.3	6.9	2184	1,4
FLAG (HI, 2 x Nyquist)	3.8	28.0, 33.5	5.2	1640	1,5

^aThe physical area of the GBT aperture is taken as 7854 m² for the calculation of SSFoM using (11).

^b $\theta_b = \frac{\lambda}{2D}$ is taken as the Nyquist beam separation.

^c T_{sys}/η for the central beam and the 6 outer beams.

^d N_{effb} is computed using (10).

NOTE—1. Ref. This paper

2. Spectroscopic observations near 1350 MHz with Nyquist ($\sim 4'$) beam separation.
3. Spectroscopic observations near 1350 MHz with twice Nyquist ($\sim 8'$) beam separation.
4. HI observations near 1420 MHz with Nyquist ($\sim 4'$) beam separation.
5. HI observations near 1420 MHz with twice Nyquist ($\sim 8'$) beam separation.

holistic approach to the design optimization of the array elements and front end electronics. Extensive modeling efforts were critical to the PAF design optimization and understanding the system performance (Warnick et al. 2011; Warnick, Woestenburg & Russer 2009; Roshi & Fisher 2016). The steps involved in the modeling are the following (Roshi & Fisher 2016). The dipole array was first modeled using a full wave finite element solver in CST microwave studio⁴ to obtain the element beam patterns and the impedance matrix. The embedded beam patterns are then obtained from the element patterns. The secondary radiation patterns for the GBT optical geometry were obtained using a physical optics approximation. The embedded patterns along with the GBT geometry were used to compute the noise covariance matrices due to ground spillover. The secondary patterns were used to compute the signal response due to the source and noise covariances due to the sky background radiation. The impedance matrix of the array combined with a noise model for the cryogenic LNAs (Pospieszalski 2010) provided the receiver noise covariance. The amplifier noise parameters used for the modeling are: minimum receiver temperature $T_{\min} = 4.2$ K, the optimum impedance $Z_{opt} = 28.9 - j3.5 \Omega$, and Lange parameter $N = 0.007$. The noise parameters are considered to be approximately constant over the frequency range 1200 to 1550 MHz. This LNA noise model is obtained from the amplifier modeling and reproduces the measured LNA noise temperature, however, we note that these parameters cannot be uniquely

Table 4. Survey speed comparison

Receiver System	A (m ²)	Freq (GHz)	θ_b^a (')	T_{sys}/η^b (K)	N_{effb}	SSFoM ^c (deg ² m ⁴ K ⁻²)	BW ^d (MHz)	SSFoM×BW (deg ² m ⁴ K ⁻² MHz)	Notes/Ref
FLAG (Nyquist)	7854	1.35	4	25.4, 25.7	6.9	2924	150	3.6×10^5	1,7
FLAG	7854	1.35	4	25.4	~ 25	10690	150	1.6×10^6	1,8
GBT L-band	7854	1.35	4	25.7	1.0	415	400	1.7×10^5	2
Parkes multi-beam	3217	1.37	5.9	41.9	13	1010	300	3.0×10^5	3,9
Arecibo ALFA	35633	1.37	1.8	35.2, 45.5	4.6	4228	300	1.3×10^6	4,10
Effelsberg 7beam	7854	1.41	3.7	45.8	7	782	300	2.3×10^5	5,11
Parkes with PAF	3217	1.31	5.9	60.0	~ 144	4025	700	2.8×10^6	6

^a $\theta_b = \frac{\lambda}{2D}$ is taken as the Nyquist beam separation for all telescopes.

^b T_{sys}/η are provided for the central beam and for all the outer beams for cases where two values are listed.

^cSurvey metric for spectroscopic observations.

^dReal time signal processing bandwidth.

NOTE—1. Ref. This paper

2. Ref. <https://science.nrao.edu/facilities/gbt/proposing/GBTpg.pdf>

3. Ref. http://www.parkes.atnf.csiro.au/observing/documentation/user_guide/pks_ug_3.html

4. Ref. http://www.naic.edu/alfa/gen_info/info_obs.shtml

5. Ref. https://eff100mwiki.mpifr-bonn.mpg.de/doku.php?id=information_for_astronomers:rx:p217mm

6. Ref. Chippendale et al. (2016). SSFoM at 1.31 GHz is obtained as $\text{SSFoV} \times \mathcal{S}_{\text{max}}^2$, where $\text{SSFoV}=1.4 \text{ deg}^2$ and $\mathcal{S}_{\text{max}} = 3217/60 = 53.6 \text{ m}^2 \text{ K}^{-1}$. $N_{\text{effb}} \sim \frac{\text{SSFoV}}{\theta_b^2} = 144$. The real-time processing bandwidth is assumed to be same as the front-end bandwidth of ~ 700 MHz.

7. FLAG with 7 formed beams placed at Nyquist ($\sim 4'$) beam separation.

8. Intrinsic SSFoM (see (7)) of FLAG obtained using the data shown in Fig. 6a. $\text{SSFoV}=0.11 \text{ deg}^2$; $N_{\text{effb}} \sim \frac{\text{SSFoV}}{\theta_b^2} = 25$.

9. 1.1 Jy K^{-1} is used for the calculation of SSFoM.

10. The region illuminated by ALFA is taken as ~ 213 m in diameter. 11 K Jy^{-1} for the central beam and 8.5 K Jy^{-1} for outer beams are used for the calculation of SSFoM.

11. Aperture efficiency of 48% used for the calculation of SSFoM.

⁴ a commercial 3D electromagnetic simulation software; <https://www.cst.com/>

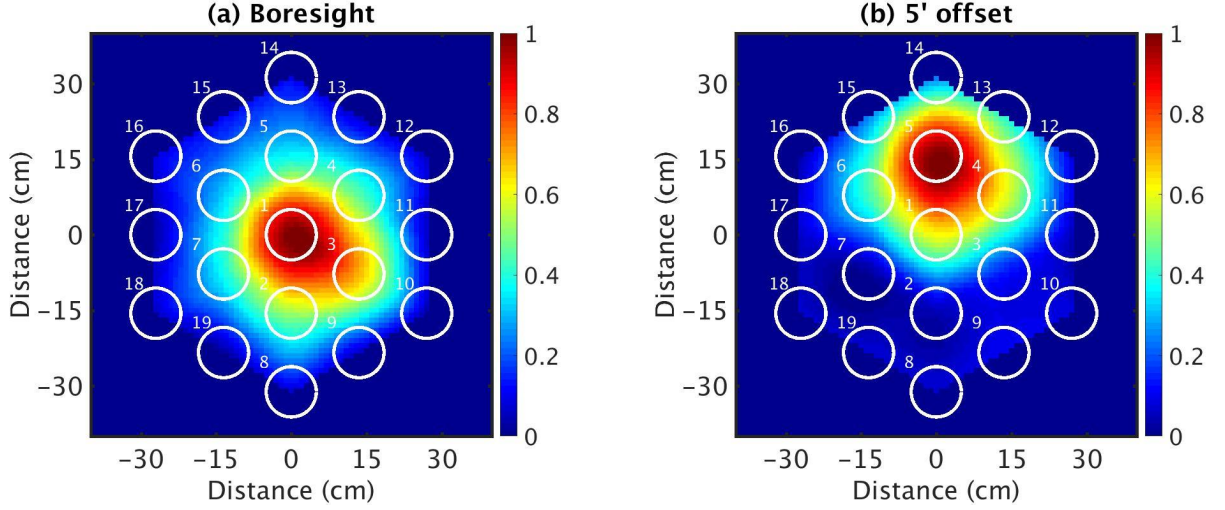


Figure 15. (a) The normalized amplitude distribution of the weights obtained for the boresight direction superposed on the dipole array geometry. The white circles indicate the location of the dipoles in the array along with the dipole number. (b) Same as (a) but for 5' offset from boresight direction.

Table 5. System parameters

Parameter	Value
Measured parameters	
T_{sys}/η near 1350 MHz	25.4 ± 2.5 K
LNA noise temperature	5 K
Inferred loss ahead of LNA ^a	2.5 K
Cosmic Microwave Background temperature	2.7 K
Galactic Background Temperature ^b	0.8 K
Estimated parameters	
Atmospheric Temperature ^c	2 K
Inferred from Model	
Beamformed Receiver temperature	7.5 K
Spillover Temperature	3.5 K
Total System Temperature	16.5 K
Estimated Spillover Efficiency	98.8%
Estimated Aperture Efficiency	60%
Model T_{sys}/η near 1350 MHz	27.5 K ^d

^aM

odel results with an additional noise of 2.5 K to account for losses ahead of the LNA (see Fig. 3b) are in qualitative agreement with the measurements for the amplifier noise parameters used here.

^bMedian of the off-source sky temperature estimated from the 1.4 GHz survey data of Reich & Reich (1986)

^cDelahaye, Gole & Waldteufel (2002)

^dThe uncertainty in the model value is up to 20% (see text)

constrained from noise temperature measurements alone. Accurate noise modeling of the LNA and the measurement of noise parameters are underway – PAF model results with these new values will be presented elsewhere. The signal response and noise covariances were used to compute the expected S/N. The maximum S/N beamformer algorithm was then used to find beamformer coefficients for each desired beam steering direction. The model was run repeatedly for a set of frequencies ranging from 1200 to 1550 MHz. With the accurate representation of the PAF by input parameters, the model can predict the receiver temperature, antenna temperature, spillover temperature, and the full polarization electromagnetic fields in the antenna aperture. Below we compare the measured system performance with PAF model predictions.

The PAF model prediction for the boresight direction is shown in Fig. 14 along with the measured median T_{sys}/η as a function of frequency ⁵ The median values were computed from the measured data points shown in Fig. 9 over a frequency interval of ~ 1.5 MHz. The median values for Y-polarization were computed from the subset of measured values that is not severely affected by the pointing offset and faulty dipoles (see Section 6.2). The model results are plotted with an additional noise contribution to T_{sys} to account for the losses ahead of the LNA. For the LNA noise parameters used here, model results with an additional noise of 2.5 K (see Fig. 3b) are in qualitative agreement with the measurements at frequencies below 1.45 GHz. The discrepancy between model and measurement at frequency above 1.45 GHz may be due to a combination of the following factors: inaccuracy in the amplifier noise parameters, error in the electromagnetic simulation, unmodeled ground scattering due to the feed support structure, or manufacturing errors in the dipoles. Ground scattering from the feed support may have additional contributions at higher frequencies where the increase in system temperature is dominated by the presence of array grating lobes. These possibilities are the subject of an ongoing investigation.

The model prediction for T_{sys}/η versus offset from the boresight is shown in the Fig. 7. The model results, obtained with the 2.5 K excess noise due to the losses upstream of the LNA (see Fig. 3b), tracks closely with the measured variation of T_{sys}/η as a function of the radial offset very well. The increase in T_{sys}/η for offsets larger than $5'$ is due to the finite size of the dipole array. This is evident from Fig. 15, where we plot the normalized beamformer weight distribution over the dipole array geometry for the boresight beam, and a beam $\sim 5'$ offset from the boresight direction. These weight distributions are obtained from grid observation data toward Virgo A. As seen in the figure, significant amplitudes for the weights are clustered around seven dipole elements, roughly following the Airy pattern due to the compact source. At offsets $\gtrsim 5'$ the cluster of seven elements is located at the edge of the array centered on dipole 5 (see Fig. 15b). Thus at offsets more than $5'$ from the boresight the dipole array does not have enough elements to sample the Airy pattern well. Thus the FoV limitation of the array indicated by the upward slope of T_{sys}/η in Fig. 7 is caused only by the limited extent of the array, and thus could be extended by the addition of more elements.

On-telescope measurements do not provide T_{sys} and η separately and so we infer these values and other system parameters from the PAF model. The inferred system parameters are summarized in Table 5. The system temperature after forming the beams is about 16 K, with contributions from receiver noise of 7.5 K, spillover of 3.5 K and sky background plus atmosphere of 5.5 K. The median increase in formed beam S/N on a compact source is about a factor of eight compared to a single dipole near 1336 MHz. This increase in S/N implies a T_{sys}/η of ~ 216 K for the single dipole case - based on scaling the measured T_{sys}/η for the formed beam (see Table 5). This high T_{sys}/η is due to the large spillover contribution when observing with a single dipole. The inferred spillover temperature from the model is ~ 100 K for the single dipole case. The spillover efficiency is increased to about 98% in the process of beamforming, thus reducing the modeled T_{sys}/η to about 27 K for the formed beam. The high ground suppression achieved for the formed beam, results in a somewhat lower aperture efficiency (about 60 %) compared to the GBT single feed system, an inevitable trade off for the 19-element prime focus PAF.

The uncertainty in the model predictions have several contributions, which include: (a) amplifier noise parameters and their frequency dependence; (b) accuracy of the CST simulation results and (c) model not accounting for the scattering due to feed support structures. The estimated values of T_{sys}/η at frequencies below ~ 1300 MHz sensitively depends on the amplifier noise parameters due to a higher level of mutual coupling in the array. At frequencies above ~ 1450 MHz the grating lobes become significant and hence the scattering due to the feed support structure could limit the accuracy of the computation. In the frequency range near 1350 MHz we estimate that the model predictions are accurate to within 20%. This estimation of accuracy is obtained by considering different amplifier noise parameters

⁵ The model curve is not a least square fit to the data. Currently, the major contribution to the uncertainty in the modeled value is the inaccuracies in one of the input parameters to the model, the amplifier noise parameters and their frequency dependence. We are in the process of accurately modeling the amplifier noise parameters and measuring them. The PAF model results based on these new measurements will be presented elsewhere.

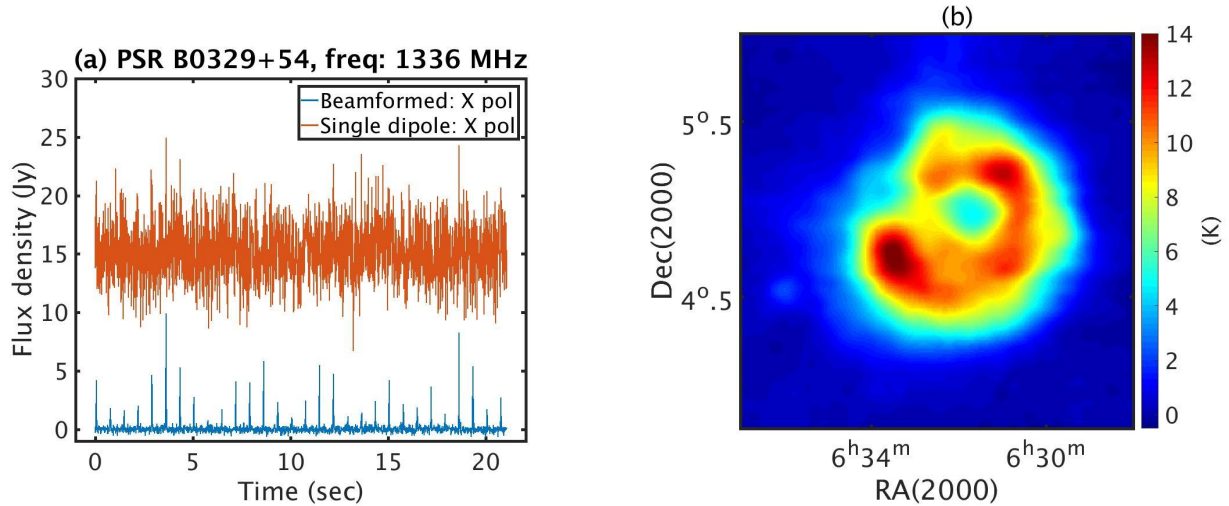


Figure 16. (a) Observation of the pulsar B0329+54 with a single dipole (top) and with maximum S/N boresight beam. The increase in S/N is about a factor of eight. (b) Image of the Rosette nebula made with the PAF near 1.336 GHz.

that are consistent with the LNA noise temperature measurements and examining the variation of the computed T_{sys}/η near 1350 MHz.

7. OBSERVATIONS OF ASTRONOMICAL SOURCES

We have observed the pulsar B0329+54 and the Rosette Nebula with the PAF system on the GBT. The data taken towards these sources were obtained using the experimental setup described in Section 2 and processed as described in the Section 3.

7.1. PSR B0329+54

The pulsar B0329+54 was observed with the PAF receiver on March 16, 2017. The observed frequency was 1336.0275 MHz with a bandwidth of 300 kHz. The pulse width of B0329+54 at 10% of the peak average pulsar amplitude is 31.4 ms (Manchester et al. 2005). Therefore, the cross correlations were integrated for about 10 ms. An on-off observation on the calibrator 3C123 was performed before taking the pulsar data in the same observing setup. The data set on the calibrator was used to obtain the beamformer weights. A time series from the pulsar data was then obtained by estimating the power using the beamformer weights for every 10 ms. This power was converted into flux density units using the calibration factor derived from the 3C123 observations. The calibrated, beamformed time series from X polarization data is shown in Fig. 16a (bottom curve). For comparison the time series obtained from the central dipole is also shown in Fig. 16a (top curve). The improvement in S/N in the formed beam output is about a factor 8, similar to what is measured from observations of calibrator sources. This indicates that the transfer of beamformer weights from calibrator observation gives the expected improvement in S/N on the target source.

7.2. Rosette Nebula

The continuum emission from Rosette Nebula was observed at frequency 1336.0275 MHz with a bandwidth of ~ 300 kHz. The telescope was moved in a raster scan mode along right ascension and declination while recording the voltages. The data from each row of the raster scan were recorded to a file and processed offline as described in Section 3. The integration time for the cross correlations was set to ~ 170 ms. The telescope speed for the raster scan was such that it moved by about $1'$ ($1/10^{\text{th}}$ of the beamwidth) in the sky during this integration time. The time stamp on the data and that on the telescope position were used to obtain the sky position corresponding to each integration time.

The synchronization between the data acquisition system and the telescope for the raster scan mode of observing was not robust. This synchronization issue had two effects: (a) the sky position derived had to be corrected manually to get the true equatorial coordinates of the observed positions; (b) we lost data for a few right ascension scans, which corresponded to a gap of about $28'$ in declination in the image. As described below, this gap is filled with data obtained from different beams of the PAF.

We observed the calibrator 3C123 along with Rosette observations in order to derive the beamformer weights. However, this data set could be used only to obtain the weights for the boresight beam and another off-boresight beam (5' in elevation toward north) due to a telescope pointing offset. The images made from these two beams had the expected sensitivity. But due to the loss of data, the image had gaps and could not be filled with the data from two beams alone. We therefore derived the beamformer weights from grid observation toward Virgo A taken 2 days before the Rosette observations. These beamformer weights did not provide the optimum signal to noise ratio due to the temporal change in instrumental gain and phase between the Virgo A and Rosette observations. The degradation in S/N was about 20%. The Virgo A data set was used to form images from different beams and to calibrate the estimated power in Jy. The PAF system did not have a calibrated noise source ahead of the LNA and hence converting the flux density scale to brightness temperature scale had some uncertainty. Further, the data from beams outside the nominal FoV of the PAF ($\sim 20'$) were used to fill the gaps in the image (see above). The calibration factor to convert Jy to brightness temperature in K had to be increased by 33% for these beams. Thus, the overall accuracy of the brightness temperature scale of the image is estimated to be about 30 %. Determining the Jy to K conversion and its stability for the PAF system are part of ongoing research work.

After calibration, a linear baseline, estimated using the data points away from the Rosette nebula, was subtracted from each right ascension scan. The variation of the mean value of the baseline from scan to scan was $\sim 10\%$, which may be due to system gain variation. The image obtained from the baseline subtracted data and after combining the data from 3 beams (central beam, a beam 9' north in elevation and a beam 9' south in elevation) is shown in Fig. 16b. The combined image is smoothed with a box function of $\sim 8' \times 8'$ in size.

The features of the Rosette nebula seen in Fig. 16b compare well with those observed earlier by [Celnik \(1985\)](#) at 1410 MHz. The manual adjustment of the sky position needed due to loss of synchronization mentioned above had resulted in a residual artifact at about 2 K level in the image. This artifact is entirely due to the synchronization between data acquisition and telescope control systems and is not due to the PAF.

8. SUMMARY AND CONCLUSION

We presented the measured performance of FLAG front-end, a new 1.4 GHz 19-element, dual-polarization, cryogenic phased array feed radio astronomy receiver built for the GBT. A brief description of the instrumentation was given, which included a novel method of implementing an unformatted digital link. The performance of the system was measured by placing the PAF at the prime focus of the GBT and observing a set of astronomical calibrators. The performance metric, T_{sys}/η , had a median value of $25.4 \text{ K} \pm 2.5 \text{ K}$ near 1350 MHz. This value is comparable to the performance of the single feed system of the GBT at 1.4 GHz. The median T_{sys}/η was higher by about 5 K near the edge of the 150 MHz bandwidth of interest, centered at 1350 MHz. The increase in T_{sys}/η at 1336 MHz at $\sim 4'$ offset, required for Nyquist sampling, was $\sim 1\%$ and at $\sim 8'$ offset was $\sim 20\%$. The distribution of T_{sys}/η in elevation and cross-elevation directions was radially symmetric. This symmetry enables the PAF to form seven high sensitivity beams within the FoV, resulting in an increase in survey speed by a factor between 2.1 and 7 depending on the observing application. The FoV of the PAF system is limited by the size of the array, as there are not enough elements to form a high sensitivity beam for offset angles $\gtrsim 5'$. The PAF model predictions qualitatively agree with the measured variation of T_{sys}/η with frequency as well as with offset from boresight. The results from the observations of a pulsar and an extended source with the PAF system on the GBT are also presented.

The results presented here were processed by a narrow-band offline processing system. Future observations will use a new real-time 150 MHz bandwidth digital signal processing system developed by FLAG collaboration. The PAF and the broadband beamformer comprise the complete FLAG instrumentation, which will enable efficient searches for pulsars and Fast Radio Bursts and observations of diffuse, extended neutral hydrogen emission in the circumgalactic medium of nearby galaxies.

The authors would like to thank Sivasankaran Srikanth, Marian Pospieszalski, Anthony Kerr, Morgan Mcleod, Bob Dickman, S. K. Pan, Brent Carlson, Bill Randolph, Mike Shannon, Gerry Petencin, Kamaljeet Saini, Greg Morris and Nicole Thisdell of the National Radio Astronomy Observatory, and Karen O'Neil, Joe Brandt, Dennis Egan, Mike Hedrick, Pat Schaffner, Roger Dickenson, Bob Anderson, Ron Maddalena and Jonah Bauserman of the Green Bank Observatory. Thanks to Lewis Ball and Brian Mason of NRAO for review of a previous version of the text. We thank

the anonymous referee for the critical comments on the manuscript, particularly on the noise correlation between the PAF beams and its effect on the survey speed.

REFERENCES

- Anantharamaiah, K. R., Deshpande, A. A., Radhakrishnan, V., Ekers, R. D., et al., 1991, *International Astronomical Union Colloquium* 131, 6
- Bannister, K. W., Shannon, R. M., Macquart, J. P., Flynn, C., et al., *ApJL*, 841, 12
- Barnes, D. G., Staveley-Smith, L., de Blok, W. J. G., Oosterloo, et al., 2001, *MNRAS*, 322, 486
- Bekhti, N. B., Flöer, L., Keller, R., Kerp, J., et al., 2016, *A&A*, 594, A116
- Celnik, W. E., 1985, *A&A*, 144, 171
- Chatterjee, S., Law, C. J., Wharton, R. S., Burke-Spolaor, S., et al. 2017, *Nature*, 541, 7635, 58
- Chippendale, A. P., Beresford, R. J., Deng, X., Leach, M., et al. 2016, *Electromagnetics in Advanced Applications (ICEAA)*, 909
- Chippendale, A. P., Brown, A. J., Beresford, R. J., Hampson, G. A., et al. 2015, *Electromagnetics in Advanced Applications (ICEAA)*, 541
- Chynoweth, K. M., Langston, G. I., Yun, M. S., Lockman, F. J., et al. 2008, *AJ*, 135, 1983
- Condon, J. J., Cotton, W. D., Greisen, E. W., Yin, Q. F., et al. 1998, *AJ*, 115, 1693
- Cortes-Medellin, G., Vishwas, A., Parshley, S. C., Campbell, D. B., et al. 2015, *IEEE Transactions on Antennas and Propagation*, 63, 2471
- de Blok, W. J. G.; Keating, K. M.; Pisano, D. J.; Fraternali, F., et al., 2014, *A&A*, 569, 68
- Delahaye, J-Y., Gole P., Waldteufel, P., 2002, *Radio Science*, 37, 1011
- DeZotti, G., Masardi, M., Negrello, M., Wall, J., 2010, *A&A Review* 18, 1
- Diao, J., Warnick, K. F., 2017. *IEEE Transactions on Antennas and Propagation*, 65, 5871
- Erickson, N. R., Narayanan, G., Bardin, J. C., Warnick, K. F., et al., 2015, *IEEE International Symposium on Antennas and Propagation*, 1514
- Fisher, J. R., Bradely, R. F., 2000, *SPIE*, 4015, 308
- Groves III, W. M., Morgan, M. A., 2017, *PASP*, 129, 085001
- Hay, S. G., Bird, T. S., 2015, *Handbook of Antenna Technologies*, Eds. Zhi Ning Chen, Springer, Singapore
- Hay, S. G., O’Sullivan, J. D., 2008, *Radio Science* 43, 6
- Hay, S. G., 2010, *International Journal of Microwave and Optical Technology* 5, 375
- Jeffs, B. D., Warnick, K. F., Landon, J., Waldron, J., et al. 2008, *IEEE Journal of Selected Topics in Signal Processing*, 2, 635
- Katz, J. I., 2016, *Modern Physics Letters A*, 31, id. 1630013
- Kereš, D., Katz, N., Fardal, M., Davé, R., et al., 2009, *MNRAS*, 395, 160
- Kereš, D., Katz, N., Weinberg, D. H., Davé, R., 2005, *MNRAS*, 363, 2
- Lorimer, D. R., Bailes, M., McLaughlin, M. A., Narkevic, D. J., et al. 2007, *Science*, 318, 777
- Manchester, R. N., 2001, *PASA*, 18, 1
- Manchester, R. N., Hobbs, G. B., Teoh, A., Hobbs, M., 2005, *AJ*, 129, 1993
<http://www.atnf.csiro.au/people/pulsar/psrcat/>
- Mihos, J. C., Keating, K. M., Holley-Bockelmann, K., Pisano, D. J. 2012, *ApJ*, 761, 186
- Morgan, M., A., Fisher, J. R., 2014, *Statistical word boundary detection in serialized data streams*. U.S. Patent No. 8,688,617
- Morgan, M. A., Fisher, J. R., Castro, J. J., 2013, *PASP*, 125, 695
- Oosterloo, T., Verheijen, M., van Cappellen, W., 2010, *ISKAF2010 Science Meeting* 1, 43
- Padman, R., 1995, *Multi-Feed Systems for Radio Telescopes*, *Astronomical Society of the Pacific Conference Series*, 75, 3
- Perley, R. A., Butler, B. J., 2017, *ApJSS*, 230, 7
- Petroff, E., Barr, E. D., Jameson, A., et al. 2016, *PASA*, 33, 45,
<http://www.astronomy.swin.edu.au/pulsar/frbcat/>
- Pisano, D. J., 2014, *AJ*, 147, 48
- Popping, A., Davé, R., Braun, R., Oppenheimer, B. D., 2009, *A&A*, 504, 15
- Pospieszalski, M. W., 2010, *IEEE Microwave Magazine*, 11, 61
- Prochaska, J. X., Herbert-Fort, S., Wolfe, A. M., 2005, *ApJ*, 635, 123
- Reich, P., Reich, W., 1986, *A&ASS*, 63, 205
- Roshi, D. A., Fisher, J. R., 2016, *NRAO Electronic Division Internal Report*, 330
- Roshi, D. A., Shillue, W., Fisher, J. R., White, S., et al. 2015, *NRAO Electronic Division Internal Report*, 326
- Sancisi, R., Fraternali, F., Oosterloo, T., van der Hulst, T., 2008, *A&A Rev.*, 15, 189

- Veidt, B., Hovey, G. J., Burgess, T., Smegal, R., J., et al. 2011, *IEEE Transactions on Antennas and Propagation*, 59, 6
- Warnick, K. F., Carter, D., Webb, T., Landon, J., et al. 2011, *IEEE Transactions on Antennas and Propagation*, 59, 1876
- Warnick, K. F., Jensen, M. A., 2007, *IEEE transactions on Antennas and Propagation* 55, 1726
- Warnick, K. F., Ivashina, M. V., Maaskant, R., Woestenburg, B., 2010, *IEEE Transactions on Antennas and Propagation* 58, 2121
- Warnick, K. F., Jeffs, B. D., 2008, *IEEE antennas and wireless propagation letters* 7, 565
- Warnick, K. F., Maaskant, R., Ivashina, M. V., Davidson, D. B., et al. 2016, *Proceedings of the IEEE* 104, 607
- Warnick, K. F., Woestenburg, B., Russer, P., 2009, *IEEE Transactions on Antennas and Propagation*, 57, 1634
- Weinreb, S., Bardin, J., Mani, H., Jones, G., 2009, *Review of Scientific Instruments*, 80, 044702
- Woestenburg, E. E. M., 2005, *Tech. Rep. RP-083*, ASTRON, Dwingeloo, The Netherlands
- Wolfe, S. A., Lockman, F. J., Pisano, D. J., 2016, *ApJ*, 816, 81
- Wolfe, S. A., Pisano, D. J., Lockman, F. J., McGaugh, S. S., et al. 2013, *Nature*, 497, 224
- Wu, Y., Jin, C., Fan, J., Zhao, X., et al., 2016, *Progress in Electromagnetic Research Symposium (PIERS)*, 1667